

## A high-level programming-language implementation of topology optimization applied to steady-state Navier–Stokes flow

Laurits Højgaard Olesen<sup>\*,†</sup>, Fridolin Okkels and Henrik Bruus

*MIC—Department of Micro and Nanotechnology, Technical University of Denmark,  
DK-2800 Kongens Lyngby, Denmark*

### SUMMARY

We present a versatile high-level programming-language implementation of non-linear topology optimization. Our implementation is based on the commercial software package FEMLAB, and it allows a wide range of optimization objectives to be dealt with easily. We exemplify our method by studies of steady-state Navier–Stokes flow problems, thus extending the work by Borrvall and Petersson on topology optimization of fluids in Stokes flow (*Int. J. Num. Meth. Fluids* 2003; **41**:77–107). We analyse the physical aspects of the solutions and how they are affected by different parameters of the optimization algorithm. A complete example of our implementation is included as FEMLAB code in an appendix. Copyright © 2005 John Wiley & Sons, Ltd.

KEY WORDS: topology optimization; Navier–Stokes flow; inertial effects; FEMLAB

### 1. INTRODUCTION

The material distribution method in topology optimization was originally developed for stiffness design of mechanical structures [1] but has now been extended to a multitude of design problems in structural mechanics as well as to optics and acoustics [2–5]. Recently Borrvall and Petersson introduced the method for fluids in Stokes flow [6]. However, it is desirable to extend the method to fluids described in a full Navier–Stokes flow; a direction pioneered by the work of Sigmund and Gersborg-Hansen [7–9].

In the present work we present such an extension by introducing a versatile high-level programming-language implementation of non-linear topology optimization, based on the commercial software package FEMLAB. It has a wider range of applicability than the Navier–Stokes

---

\*Correspondence to: Laurits Højgaard Olesen, MIC—Department of Micro and Nanotechnology, DTU Bldg. 345 East, Technical University of Denmark, DK-2800 Kongens Lyngby, Denmark.

†E-mail: lho@mic.dtu.dk

problems studied here, and moreover it allows a wide range of optimization objectives to be dealt with easily.

Extending the topology optimization method to new physical domains generally involves some rethinking of the design problem and some 'trial and error' to determine suitable design objectives. It also requires the numerical analysis and implementation of the problem, e.g. using the finite element method (FEM). This process is accelerated a lot by using a high-level FEM library or package that allows different physical models to be joined and eases the tasks of geometry setup, mesh generation, and postprocessing. The disadvantage is that high-level packages tend to have rather complex data structure, not easily accessible to the user. This can complicate the actual implementation of the problem because the sensitivity analysis is traditionally formulated in a low-level manner.

In this work we have used the commercial finite-element package FEMLAB both for the solution of the flow problem and for the sensitivity analysis required by the optimization algorithm. We show how this sensitivity analysis can be performed in a simple way that is almost independent of the particular physical problem studied. This approach proves even more useful for multi-field extensions, where the flow problem is coupled to, e.g. heat conduction, convection–diffusion of solutes, and deformation of elastic channel walls in valves and flow rectifiers [10].

The paper is organized as follows: In Section 2 we introduce the topology optimization method for fluids in Navier–Stokes flow, and discuss the objective of designing fluidic devices or channel networks for which the power dissipation is minimized. In Section 3 we express the Navier–Stokes equations in a generic divergence form that allows them to be solved with FEMLAB. This form encompasses a wide range of physical problems. We also work out the sensitivity analysis for a class of integral-type optimization objectives in such a way that the built-in symbolic differentiation tools of FEMLAB can be exploited. In Section 4 we present our two numerical examples that illustrates different aspects and problems to consider: The first example deals with designing a structure that can guide the flow in the reverse direction of an applied pressure drop. The general outcome of the optimization is an *S*-shaped channel, but the example illustrates how the detailed structure depends on the choice of the parameters of the algorithm. The second example deals with a four terminal device where the fluidic channel design that minimizes the power dissipation shows a Reynolds number dependence. As the Reynolds number is increased a transition occurs between two topologically different solutions, and we discuss how the position of the transition depends on the choice of initial conditions. Finally in the appendix we include a transcript of our FEMLAB code required for solving the second numerical example. The code amounts to 111 lines—excluding the optimization algorithm that can be obtained by contacting Svanberg [11–13].

## 2. TOPOLOGY OPTIMIZATION FOR NAVIER–STOKES FLOW IN STEADY STATE

Although our high-level programming-language implementation is generally applicable we have chosen to start on the concrete level by treating the basic equations for our main example: the full steady-state Navier–Stokes flow problem for incompressible fluids.

We consider a given computational domain  $\Omega$  with appropriate boundary conditions for the flow given on the domain boundary  $\partial\Omega$ . The goal of the optimization is to distribute a certain amount of solid material inside  $\Omega$  such that the material layout defines a fluidic device or

channel network that is optimal with respect to some objective, formulated as a function of the variables, e.g. minimization of the power dissipated inside the domain.

The basic principle in the material distribution method for topology optimization is to replace the original discrete design problem with a continuous one where the material density is allowed to vary continuously between solid and void [2]. Thus in our flow problem we assume the design domain to be filled with some idealized porous material of spatially varying permeability. Solid wall and open channels then correspond to the limits of very low and very high permeability, respectively.

In the final design there should preferably be no regions at intermediate permeability since otherwise it cannot be interpreted as a solution to the original discrete problem. Alternatively it may be possible to fabricate the device from polymeric materials such as PDMS that naturally have a finite permeability to the fluid [14].

2.1. Governing equations for flow in idealized porous media

We assume that the fluid flowing in the idealized porous medium is subject to a friction force  $\mathbf{f}$  which is proportional to the fluid velocity  $\mathbf{v}$ , c.f. Darcy’s law. Thus  $\mathbf{f} = -\alpha\mathbf{v}$ , where  $\alpha(\mathbf{r})$  is the inverse of the local permeability of the medium at position  $\mathbf{r}$ . These properties of the idealized porous medium may only be approximately valid for an actual medium. However, the assumptions are not in conflict with any fundamental physical law, and since the converged solutions contain only solid walls and open channels, the specific nature of the idealized porous medium is of no consequence.

The flow problem is described in terms of the fluid velocity field  $\mathbf{v}(\mathbf{r})$  and pressure  $p(\mathbf{r})$ . The governing equations are the steady state Navier–Stokes equation and the incompressibility constraint

$$\rho(\mathbf{v} \cdot \nabla)\mathbf{v} = \nabla \cdot \boldsymbol{\sigma} - \alpha\mathbf{v} \tag{1}$$

$$\nabla \cdot \mathbf{v} = 0 \tag{2}$$

where  $\rho$  is the mass density of the fluid. For an incompressible Newtonian fluid the components  $\sigma_{ij}$  of the Cauchy stress tensor  $\boldsymbol{\sigma}$  are given by

$$\sigma_{ij} = -p\delta_{ij} + \eta \left( \frac{\partial v_i}{\partial x_j} + \frac{\partial v_j}{\partial x_i} \right) \tag{3}$$

where  $\eta$  is the dynamic viscosity. The formalism is valid in three dimensions, but for simplicity we shall consider only two-dimensional problems, i.e. we assume translational invariance in the third dimension and set  $\mathbf{r} = (x_1, x_2)$  and  $\mathbf{v} = (v_1(\mathbf{r}), v_2(\mathbf{r}))$ . The boundary conditions will typically be either Dirichlet type specifying the velocity field  $\mathbf{v}$  on the boundary or Neumann type specifying the external forces  $\mathbf{n} \cdot \boldsymbol{\sigma}$ .

It is convenient to introduce a design variable field  $\gamma(\mathbf{r})$  controlling the local permeability of the medium. We let  $\gamma$  vary between zero and unity, with  $\gamma=0$  corresponding to solid material and  $\gamma=1$  to no material. Following Reference [6] we then relate the local inverse permeability  $\alpha(\mathbf{r})$  to the design field  $\gamma(\mathbf{r})$  by the convex interpolation

$$\alpha(\gamma) \equiv \alpha_{\min} + (\alpha_{\max} - \alpha_{\min}) \frac{q[1 - \gamma]}{q + \gamma} \tag{4}$$

where  $q$  is a real and positive parameter used to tune the shape of  $\alpha(\gamma)$ . Ideally, impermeable solid walls would be obtained with  $\alpha_{\max} = \infty$ , but for numerical reasons we need to choose a finite value for  $\alpha_{\max}$ . For the minimal value we choose  $\alpha_{\min} = 0$ .<sup>‡</sup>

For a given material distribution  $\gamma(\mathbf{r})$  there are two dimensionless numbers characterizing the flow, namely the Reynolds number

$$Re = \frac{\rho \ell v}{\eta} \quad (5)$$

describing the ratio between inertia and viscous forces, and the Darcy number

$$Da = \frac{\eta}{\alpha_{\max} \ell^2} \quad (6)$$

describing the ratio between viscous and porous friction forces. Here  $\ell$  is a characteristic length scale of the system and  $v$  a characteristic velocity.

Almost impermeable solid material is obtained for very low Darcy numbers, in practice  $Da \lesssim 10^{-5}$ . Further insight into the meaning of the Darcy number is gained by considering Poiseuille flow in a channel or slit of width  $\ell$  between two infinite parallel plates of porous material. In this case the fluid velocity inside the porous walls decays on a length scale  $\ell_{Da}$ , where  $\ell_{Da} = \sqrt{Da} \ell = \sqrt{\eta/\alpha_{\max}}$ . See also Section 4.1.1 for details on how the flow depends on  $Da$ .

## 2.2. Power dissipation

In the pioneering work by Borrvall and Petersson [6] the main focus was on minimizing the power dissipation in the fluid. The total power  $\Phi$  dissipated inside the fluidic system (per unit length in the third dimension) is given by [15]

$$\Phi(\mathbf{v}, p, \gamma) = \int_{\Omega} \left[ \frac{1}{2} \eta \sum_{i,j} \left( \frac{\partial v_i}{\partial x_j} + \frac{\partial v_j}{\partial x_i} \right)^2 + \sum_i \alpha(\gamma) v_i^2 \right] d\mathbf{r} \quad (7a)$$

In steady-state this is equal to the sum of the work done on the system by the external forces and the kinetic energy convected into it

$$\Phi(\mathbf{v}, p, \gamma) = \int_{\partial\Omega} \sum_{i,j} \left[ n_i \sigma_{ij} v_j - n_i v_i \left( \frac{1}{2} \rho v_j^2 \right) \right] ds \quad (7b)$$

Here  $\mathbf{n}$  is a unit outward normal vector such that  $\mathbf{n} \cdot \boldsymbol{\sigma}$  is the external force acting on the system boundary and  $\mathbf{n} \cdot \boldsymbol{\sigma} \cdot \mathbf{v}$  is the work done on the system by this force. Moreover, in the common case where the geometry and boundary conditions are such that the no-slip condition  $\mathbf{v} = \mathbf{0}$

<sup>‡</sup>Borrvall and Petersson suggest a model for plane flow between two parallel surfaces of varying separation  $h(\mathbf{r})$ . The power dissipation due to out-of-plane shears is modelled by an absorption term  $-\alpha \mathbf{v}$ , where  $\mathbf{v}(\mathbf{r})$  is the average velocity between the surfaces and  $\alpha(\mathbf{r}) = 12\eta/h(\mathbf{r})^2$ . In their model it is therefore natural to operate with a non-zero  $\alpha_{\min} = 12\eta/h_{\max}^2$  in Equation (4).

applies on all external solid walls, while on the inlet and outlet boundaries  $\mathbf{v}$  is parallel to  $\mathbf{n}$  and  $(\mathbf{n} \cdot \nabla) \mathbf{v} = 0$ ,<sup>§</sup> Equation (7b) reduces to

$$\Phi(\mathbf{v}, p, \gamma) = \int_{\partial\Omega} -\mathbf{n} \cdot \mathbf{v} \left( p + \frac{1}{2} \rho v^2 \right) ds \quad (7c)$$

Borrvall and Petersson showed that for Stokes flow with Dirichlet boundary conditions everywhere on the boundary  $\partial\Omega$ , the problem of minimizing the total power dissipation inside the fluidic device subject to a volume constraint on the material distribution is mathematically well-posed. Moreover it was proven that in the case where  $\alpha(\gamma)$  is a linear function, the optimal material distribution is fully discrete-valued.

When  $\alpha(\gamma)$  is not linear but *convex* then the solid/void interfaces in the optimal solution are not discrete zero/unity transitions but slightly smeared out. Convexity implies that the (negative value of the) slope of  $\alpha$  at  $\gamma=0$  is larger than at  $\gamma=1$ ; therefore there will be a neighbourhood around the discrete interface where it pays to move material from the solid side to the void. Using the interpolation in Equation (4) we have  $\alpha'(0) = (\alpha_{\min} - \alpha_{\max})(1+q)/q$  and  $\alpha'(1) = (\alpha_{\min} - \alpha_{\max})q/(1+q)$ . For large values of  $q$  the interpolation is almost linear and we expect almost discrete interfaces, whereas for small  $q$  we expect smeared out interfaces in the optimized solution.

Consider the case when Equation (7c) applies. If the system is driven with a prescribed flow rate then minimizing the total power dissipation is clearly equivalent to minimizing the pressure drop across the system. Conversely, if the system is driven at a prescribed pressure drop, then the natural design objective will be to maximize the flow rate which is equivalent to maximizing the dissipated power, c.f. Equation (7c). In either case the objective can be described as minimizing the *hydraulic resistance* of the system.

For problems with more complex design objectives, such as a minimax problem for the flow rate through several different outlets, there will typically be no analog in terms of total dissipated power. In such cases there is no guarantee for the existence of a unique optimal solution and one has to be extra careful when formulating the design problem.

### 3. GENERALIZED FORMULATION OF THE OPTIMIZATION PROBLEM

For a given material distribution we solve the Navier–Stokes flow problem using the commercial finite element software FEMLAB. It provides both a graphical front-end and a library of high-level scripting tools based on the MATLAB programming language, and it allows the user to solve a wide range of physical problems by simply typing in the strong form of the governing equations as text expressions. The equations must then comply with a generic divergence form that eases the conversion to weak form required for the finite element solution. However, that is not a severe constraint since this is the natural way of expressing most partial differential equations originating from conservation laws.

Since we have chosen fluidics as our main example, we begin by expressing the incompressible Navier–Stokes flow problem in divergence form. Then we state the optimization problem

<sup>§</sup>In particular this is the case when the inlets and outlets are chosen as straight channels sufficiently long that prescribing a parabolic Poiseuille profile can be justified, see Figures 1 and 6.

with a general form of the design objective function and perform the discretization and sensitivity analysis based on this generalized formulation. We stress that although for clarity our examples are formulated in two dimensions only, the method is fully applicable for 3D systems.

### 3.1. The flow problem in divergence form

We first introduce the velocity–pressure vector  $\mathbf{u} = [v_1, v_2, p]$  and define for  $i = 1, 2, 3$  the quantities  $\mathbf{\Gamma}_i$  and  $F_i$  as

$$\mathbf{\Gamma}_1 \equiv \begin{bmatrix} \sigma_{11} \\ \sigma_{21} \end{bmatrix}, \quad \mathbf{\Gamma}_2 \equiv \begin{bmatrix} \sigma_{12} \\ \sigma_{22} \end{bmatrix}, \quad \mathbf{\Gamma}_3 \equiv \begin{bmatrix} 0 \\ 0 \end{bmatrix} \quad (8)$$

and

$$F_1 \equiv \rho(\mathbf{v} \cdot \nabla)v_1 + \alpha(\gamma)v_1, \quad F_2 \equiv \rho(\mathbf{v} \cdot \nabla)v_2 + \alpha(\gamma)v_2, \quad F_3 \equiv \nabla \cdot \mathbf{v} \quad (9)$$

Using this, Equations (1) and (2) can be written in divergence form as

$$\nabla \cdot \mathbf{\Gamma}_i = F_i \quad \text{in } \Omega, \quad \text{Governing equations} \quad (10a)$$

$$R_i = 0 \quad \text{on } \partial\Omega, \quad \text{Dirichlet b.c.} \quad (10b)$$

$$-\mathbf{n} \cdot \mathbf{\Gamma}_i = G_i + \sum_{j=1}^3 \frac{\partial R_j}{\partial u_i} \mu_j \quad \text{on } \partial\Omega, \quad \text{Neumann b.c.} \quad (10c)$$

where  $\mathbf{\Gamma}_i$  and  $F_i$  are understood to be functions of the solution  $\mathbf{u}$ , its gradient  $\nabla \mathbf{u}$ , and of the design variable  $\gamma$ . The quantity  $R_i(\mathbf{u}, \gamma)$  in Equation (10b) describes Dirichlet type boundary conditions. For example, fluid no-slip boundary conditions are obtained by defining  $R_1 \equiv v_1$  and  $R_2 \equiv v_2$  on the external solid walls. The quantity  $G_i(\mathbf{u}, \gamma)$  in Equation (10c) describe Neumann type boundary conditions, and  $\mu_i$  denote the Lagrange multiplier necessary to enforce the constraint  $R_i = 0$ , e.g. the force with which the solid wall has to act upon the fluid to enforce the no-slip boundary condition. Of course, it is not possible to enforce both Dirichlet and Neumann boundary conditions for the same variable simultaneously. Only when the variable  $u_i$  is not fixed by any of the Dirichlet constraints  $R_j$  does the Neumann condition  $G_i$  come into play, as all  $\partial R_j / \partial u_i$  vanish and the Lagrange multipliers  $\mu_j$  are decoupled from Equation (10c). Inactive Dirichlet constraints can be obtained simply by specifying the zero-function  $R_i \equiv 0$ , that also satisfies Equation (10b) trivially.

### 3.2. The objective function

In general the design objective for the optimization is stated as the minimization of a certain *objective function*  $\Phi(\mathbf{u}, \gamma)$ . We shall consider a generic integral-type objective function of the form

$$\Phi(\mathbf{u}, \gamma) = \int_{\Omega} A(\mathbf{u}, \gamma) \, d\mathbf{r} + \int_{\partial\Omega} B(\mathbf{u}, \gamma) \, ds \quad (11)$$

In particular, we can treat the design objective of minimizing the power dissipation inside the fluidic domain by taking, c.f. Equation (7a)

$$A \equiv \frac{1}{2} \eta \sum_{i,j} \left( \frac{\partial v_i}{\partial x_j} + \frac{\partial v_j}{\partial x_i} \right)^2 + \sum_i \alpha(\gamma) v_i^2 \quad \text{in } \Omega \quad \text{and} \quad B \equiv 0 \quad \text{on } \partial\Omega \tag{12}$$

Alternatively, the objective of maximizing the flow out through a particular boundary segment  $\partial\Omega_o$  is obtained by choosing

$$A \equiv 0 \quad \text{in } \Omega \quad \text{and} \quad B \equiv \begin{cases} -\mathbf{n} \cdot \mathbf{v} & \text{on } \partial\Omega_o \\ 0 & \text{on } \partial\Omega \setminus \partial\Omega_o \end{cases} \tag{13}$$

and objectives related to  $N$  discrete points  $\mathbf{r}_k$  can be treated using Dirac delta functions as

$$A \equiv \sum_{k=1}^N A_k(\mathbf{u}, \gamma) \delta(\mathbf{r} - \mathbf{r}_k) \quad \text{in } \Omega \quad \text{and} \quad B \equiv 0 \quad \text{on } \partial\Omega \tag{14}$$

Finally we stress that not all optimization objectives lend themselves to be expressed in the form of Equation (11)—an example of which is the problem of maximizing the lowest vibrational eigenfrequency in structural mechanics.

### 3.3. Optimization problem

The optimal design problem can now be stated as a continuous constrained non-linear optimization problem

$$\min_{\gamma} \Phi(\mathbf{u}, \gamma) \tag{15a}$$

$$\text{subject to: } \int_{\Omega} \gamma(\mathbf{r}) d\mathbf{r} - \beta|\Omega| \leq 0, \quad \text{Volume constraint} \tag{15b}$$

$$: 0 \leq \gamma(\mathbf{r}) \leq 1, \quad \text{Design variable bounds} \tag{15c}$$

$$: \text{Equations (10a)–(10c),} \quad \text{Governing equations} \tag{15d}$$

With the volume constraint we require that at least a fraction  $1 - \beta$  of the total volume  $|\Omega|$  should be filled with porous material.

The very reason for replacing the original discrete design problem with a continuous one by assuming a porous and permeable material, is that it allows the use of efficient mathematical programming methods for smooth problems. We have chosen the popular method of moving asymptotes (MMA) [11, 12], which is designed for problems with a large number of degrees-of-freedom and thus well-suited for topology optimization [2]. It is a gradient-based algorithm requiring information about the derivative with respect to  $\gamma$  of both the objective function  $\Phi$  and the constraints. Notice that for any  $\gamma$  the governing equations allow us to solve for  $\mathbf{u}$ ; therefore in effect they define  $\mathbf{u}[\gamma]$  as an implicit function. The gradient of  $\Phi$  is then obtained using the chain rule

$$\frac{d}{d\gamma} [\Phi(\mathbf{u}[\gamma], \gamma)] = \frac{\partial \Phi}{\partial \gamma} + \int_{\Omega} \frac{\partial \Phi}{\partial \mathbf{u}} \cdot \frac{\partial \mathbf{u}}{\partial \gamma} d\mathbf{r} \tag{16}$$

However, because  $\mathbf{u}[\gamma]$  is implicit, it is impractical to evaluate the derivative  $\partial\mathbf{u}/\partial\gamma$  directly. Instead, we use the adjoint method to eliminate it from Equation (16) by computing a set of Lagrange multipliers for Equations (10a)–(10c) considered as constraints [16]. For details see Section 3.4.

The optimization process is iterative and the  $k$ th iteration consists of three steps:

- (i) Given a guess  $\gamma^{(k)}$  for the optimal material distribution we first solve Equations (10a)–(10b) for  $\mathbf{u}^{(k)}$  as a finite element problem using FEMLAB.
- (ii) Next, the sensitivity analysis is performed where the gradient of the objective and constraints with respect to  $\gamma$  is evaluated. In order to eliminate  $\partial\mathbf{u}/\partial\gamma$  from Equation (16) we solve the adjoint problem of Equations (10a)–(10c) for the Lagrange multipliers  $\tilde{\mathbf{u}}^{(k)}$ , also using FEMLAB.
- (iii) Finally, we use MMA to obtain a new guess  $\gamma^{(k+1)}$  for the optimal design based on the gradient information and the past iteration history.

Of the three steps, (i) is the most expensive computationalwise since it involves the solution of a non-linear partial differential equation.

#### 3.4. Discretization and sensitivity analysis

The starting point of the finite element analysis is to approximate the solution component  $u_i$  on a set of finite element basis functions  $\{\varphi_{i,n}(\mathbf{r})\}$

$$u_i(\mathbf{r}) = \sum_n u_{i,n} \varphi_{i,n}(\mathbf{r}) \quad (17)$$

where  $u_{i,n}$  are the expansion coefficients. Similarly, the design variable field  $\gamma(\mathbf{r})$  is expressed as

$$\gamma(\mathbf{r}) = \sum_n \gamma_n \varphi_{4,n}(\mathbf{r}) \quad (18)$$

For our incompressible Navier–Stokes problem we use the standard Taylor–Hood element pair with quadratic velocity approximation and linear pressure. For the design variable we have chosen the linear Lagrange element.<sup>¶</sup>

The problem Equations (10a)–(10c) is discretized by the Galerkin method and takes the form

$$\mathbf{L}_i(\mathbf{U}, \boldsymbol{\gamma}) - \sum_{j=1}^3 \mathbf{N}_{ji}^T \boldsymbol{\Lambda}_j = \mathbf{0} \quad \text{and} \quad \mathbf{M}_i(\mathbf{U}, \boldsymbol{\gamma}) = \mathbf{0} \quad (19)$$

where  $\mathbf{U}_i$ ,  $\boldsymbol{\Lambda}_i$ , and  $\boldsymbol{\gamma}$  are column vectors holding the expansion coefficients for the solution  $u_{i,n}$ , the Lagrange multipliers  $\mu_{i,n}$ , and the design variable field  $\gamma_n$ , respectively. The column vector  $\mathbf{L}_i$  contains the projection of Equation (10c) onto  $\varphi_{i,n}$  which upon partial integration

<sup>¶</sup>Another common choice is the discontinuous and piecewise constant element for the design variable. Notice that for second and higher order Lagrange elements the condition  $0 \leq \gamma_n \leq 1$  does not imply  $0 \leq \gamma(\mathbf{r}) \leq 1$  for all  $\mathbf{r}$  because of overshoot at sharp zero-to-unity transitions in  $\gamma$ . This in turn can result in negative  $\alpha$ , c.f. Equation (4), which is unphysical and also destroys the convergence of the algorithm.

is given by

$$\mathbf{L}_{i,n} = \int_{\Omega} (\varphi_{i,n} F_i + \nabla \varphi_{i,n} \cdot \boldsymbol{\Gamma}_i) \, \mathbf{dr} + \int_{\partial\Omega} \varphi_{i,n} G_i \, \mathbf{ds} \tag{20}$$

The column vector  $\mathbf{M}_i$  contains the pointwise enforcement of the Dirichlet constraint Equation (10b)

$$\mathbf{M}_{i,n} = R_i(\mathbf{u}(\mathbf{r}_{i,n})) \tag{21}$$

Finally, the matrix  $\mathbf{N}_{ij} = -\partial\mathbf{M}_i/\partial\mathbf{U}_j$  describes the coupling to the Lagrange multipliers in Equation (10c). The solution of the non-linear system in Equation (19) above corresponds to step (i) in  $k$ th iteration. The sensitivity analysis in step (ii) requires us to compute

$$\frac{d}{d\gamma}[\Phi(\mathbf{U}(\gamma), \gamma)] = \frac{\partial\Phi}{\partial\gamma} + \sum_{i=1}^3 \frac{\partial\Phi}{\partial\mathbf{U}_i} \frac{\partial\mathbf{U}_i}{\partial\gamma} \tag{22a}$$

which is done using the standard adjoint method [16]. By construction we have for any  $\gamma$  that  $\mathbf{L}_i(\mathbf{U}(\gamma), \gamma) - \sum_{j=1}^3 \mathbf{N}_{ji}^T \boldsymbol{\Lambda}_j(\gamma) = \mathbf{0}$  and  $\mathbf{M}_i(\mathbf{U}(\gamma), \gamma) = \mathbf{0}$ . Therefore also the derivative of those quantities with respect to  $\gamma$  is zero, and adding any multiple, say  $\tilde{\mathbf{U}}_i$  and  $\tilde{\boldsymbol{\Lambda}}_i$ , of them to Equation (22a) does not change the result

$$\begin{aligned} \frac{d}{d\gamma}[\Phi(\mathbf{U}(\gamma), \gamma)] &= \frac{\partial\Phi}{\partial\gamma} + \sum_{i=1}^3 \frac{\partial\Phi}{\partial\mathbf{U}_i} \frac{\partial\mathbf{U}_i}{\partial\gamma} + \sum_{i=1}^3 \left[ \tilde{\mathbf{U}}_i^T \frac{\partial}{\partial\gamma} \left( \mathbf{L}_i - \sum_{j=1}^3 \mathbf{N}_{ji}^T \boldsymbol{\Lambda}_j \right) - \tilde{\boldsymbol{\Lambda}}_i^T \frac{\partial}{\partial\gamma} (\mathbf{M}_i) \right] \\ &= \frac{\partial\Phi}{\partial\gamma} + \sum_{i=1}^3 \left( \tilde{\mathbf{U}}_i^T \frac{\partial\mathbf{L}_i}{\partial\gamma} - \tilde{\boldsymbol{\Lambda}}_i^T \frac{\partial\mathbf{M}_i}{\partial\gamma} \right) + \sum_{i=1}^3 \left[ \frac{\partial\Phi}{\partial\mathbf{U}_i} + \sum_{j=1}^3 \left( \tilde{\mathbf{U}}_j^T \frac{\partial\mathbf{L}_j}{\partial\mathbf{U}_i} + \tilde{\boldsymbol{\Lambda}}_j^T \mathbf{N}_{ji} \right) \right] \frac{\partial\mathbf{U}_i}{\partial\gamma} \\ &\quad - \sum_{i=1}^3 \left[ \sum_{j=1}^3 \tilde{\mathbf{U}}_j^T \mathbf{N}_{ij}^T \right] \frac{\partial\boldsymbol{\Lambda}_i}{\partial\gamma} \end{aligned} \tag{22b}$$

Here we see that the derivatives  $\partial\mathbf{U}_i/\partial\gamma$  and  $\partial\boldsymbol{\Lambda}_i/\partial\gamma$  of the implicit functions can be eliminated by choosing  $\tilde{\mathbf{U}}_i$  and  $\tilde{\boldsymbol{\Lambda}}_i$  such that

$$\sum_{j=1}^3 (\mathbf{K}_{ji}^T \tilde{\mathbf{U}}_j - \mathbf{N}_{ji}^T \tilde{\boldsymbol{\Lambda}}_j) = \frac{\partial\Phi}{\partial\mathbf{U}_i} \quad \text{and} \quad \sum_{j=1}^3 \mathbf{N}_{ij} \tilde{\mathbf{U}}_j = \mathbf{0} \tag{23}$$

where we introduced  $\mathbf{K}_{ij} = -\partial\mathbf{L}_i/\partial\mathbf{U}_j$ . This problem is the adjoint of Equation (19) and  $\tilde{\mathbf{U}}$  and  $\tilde{\boldsymbol{\Lambda}}$  are the corresponding Lagrange multipliers.

In deriving Equation (22b) we implicitly assumed that  $\mathbf{N}_{ij}$  is independent of  $\gamma$ , i.e. that the constraint  $R_i(\mathbf{u}, \gamma)$  is a linear function. If this is not true then the gradient  $\partial\Phi/\partial\gamma$  computed from Equation (22b) is not exact, which may lead to poor performance of the optimization algorithm if the constraints are strongly non-linear. In order to avoid such problems it is necessary to include the non-linear parts of the constraint vector  $\mathbf{M}$  into  $\mathbf{L}$  and move the corresponding Lagrange multipliers from  $\boldsymbol{\Lambda}$  into  $\mathbf{U}$ . While this is beyond the scope of the divergence form

discussed in Section 3.1, it is certainly possible to deal with such problems in FEMLAB. Also the sensitivity analysis above remains valid since it relies only on the basic form of Equation (19) for the discretized problem.

### 3.5. Implementation aspects

We end this section by discussing a few issues on the implementation of topology optimization using FEMLAB.

Firstly there is the question of how to represent the design variable  $\gamma(\mathbf{r})$ . The governing equations as expressed by  $\Gamma_i$  and  $F_i$  in Equation (10a) depend not only on the solution  $\mathbf{u}$  but also on  $\gamma$ , and the implementation should allow for this dependence in an efficient way. Here our simple and straightforward approach is to include  $\gamma$  as an extra dependent variable on equal footing with the velocity field and pressure, i.e. we append it to the velocity–pressure vector, redefining  $\mathbf{u}$  as

$$\mathbf{u} \equiv [v_1, v_2, p, \gamma] \tag{24}$$

This was already anticipated when we denoted the basis set for  $\gamma$  by  $\{\phi_{4,n}(\mathbf{r})\}$ . By making  $\gamma$  available as a field variable we can take full advantage of all the symbolic differentiation, matrix, and postprocessing tools for analysing and displaying the material distribution. Appending  $\gamma$  to the list of dependent variables we are required to define a fourth governing equation. However, since we are never actually going to solve this equation, but rather update  $\gamma$  based on the MMA step, we simply define

$$\Gamma_4 \equiv \begin{bmatrix} 0 \\ 0 \end{bmatrix}, \quad F_4 \equiv 0, \quad G_4 \equiv 0, \quad R_4 \equiv 0. \tag{25}$$

It is crucial then that the finite element solver allows different parts of the problem to be solved in a decoupled manner, i.e. it must be possible to solve Equations (10a)–(10c) for  $u_i$  for  $i = 1, 2, 3$  while keeping  $u_4$ , i.e.  $\gamma$ , fixed.

In FEMLAB the non-linear problem Equation (19) is solved using damped Newton iterations [17]. Therefore, the matrices  $\mathbf{K}_{ij} = -\partial \mathbf{L}_i / \partial \mathbf{U}_j$  and  $\mathbf{N}_{ij} = -\partial \mathbf{M}_i / \partial \mathbf{U}_j$  appearing in the adjoint problem Equation (23) are computed automatically as part of the solution process and can be obtained directly as MATLAB sparse matrices. They are given by

$$\begin{aligned} \mathbf{K}_{ij,nm} = & - \int_{\Omega} \left( \varphi_{i,n} \left[ \frac{\partial F_i}{\partial u_j} \varphi_{j,m} + \frac{\partial F_i}{\partial \nabla u_j} \cdot \nabla \varphi_{j,m} \right] + \nabla \varphi_{i,n} \right. \\ & \left. \cdot \left[ \frac{\partial \Gamma_i}{\partial u_j} \varphi_{j,m} + \frac{\partial \Gamma_i}{\partial \nabla u_j} \cdot \nabla \varphi_{j,m} \right] \right) d\mathbf{r} - \int_{\partial\Omega} \varphi_{i,n} \frac{\partial G_i}{\partial u_j} \varphi_{j,m} ds \end{aligned} \tag{26}$$

and

$$\mathbf{N}_{ij,nm} = - \left. \frac{\partial R_i}{\partial u_j} \right|_{\mathbf{r}_{i,n}} \varphi_{j,m}(\mathbf{r}_{i,n}) \tag{27}$$

Regarding the right-hand side vector  $\partial\Phi/\partial\mathbf{U}_i$  in Equation (23), notice that for a general objective as Equation (11), it has the form

$$\frac{\partial\Phi}{\partial u_{i,n}} = \int_{\Omega} \left( \frac{\partial A}{\partial u_i} + \frac{\partial A}{\partial \nabla u_i} \cdot \nabla \right) \varphi_{i,n} \, d\mathbf{r} + \int_{\partial\Omega} \frac{\partial B}{\partial u_i} \varphi_{i,n} \, ds \tag{28}$$

It is not in the spirit of a high-level finite element package to program the assembly of this vector by hand. Instead we employ the built-in assembly subroutine of FEMLAB. We construct a copy of the original problem sharing the geometry, finite element mesh, and degree-of-freedom numbering with the original. Only we replace the original fields  $\Gamma_i$ ,  $F_i$ , and  $G_i$  with

$$\tilde{\Gamma}_i \equiv \frac{\partial A}{\partial \nabla u_i}, \quad \tilde{F}_i \equiv \frac{\partial A}{\partial u_i} \quad \text{and} \quad \tilde{G}_i \equiv \frac{\partial B}{\partial u_i} \tag{29}$$

Assembling the right-hand-side vector  $\tilde{\mathbf{L}}_i$  with this definition yields exactly Equation (28), c.f. Equation (20). An extra convenience in FEMLAB is that we can rely on the built-in symbolic differentiation tools to compute the derivatives  $\partial A/\partial u_i$ , etc. In order to try out a new objective for the optimization problem, the user essentially only needs to change the text expressions defining the quantities  $A$  and  $B$ .

After solving the adjoint problem Equation (23) for  $\tilde{\mathbf{U}}_i$  and  $\tilde{\mathbf{\Lambda}}_i$  to eliminate  $\partial\mathbf{U}_i/\partial\gamma$  and  $\partial\mathbf{\Lambda}_i/\partial\gamma$  for  $i = 1, 2, 3$  in Equation (22b) we can evaluate the sensitivity

$$\begin{aligned} \frac{d}{d\gamma} [\Phi(\mathbf{U}, \gamma)] &= \frac{\partial\Phi}{\partial\gamma} + \sum_{j=1}^3 \left( \frac{\partial\mathbf{L}_j}{\partial\gamma} \right)^T \tilde{\mathbf{U}}_j - \left( \frac{\partial\mathbf{M}_j}{\partial\gamma} \right)^T \tilde{\mathbf{\Lambda}}_j \\ &= \tilde{\mathbf{L}}_4 - \sum_{j=1}^3 (\mathbf{K}_{j4}^T \tilde{\mathbf{U}}_j - \mathbf{N}_{j4}^T \tilde{\mathbf{\Lambda}}_j) \end{aligned} \tag{30}$$

where  $\mathbf{K}_{i4} = -\partial\mathbf{L}_i/\partial\gamma$ ,  $\mathbf{N}_{i,4} = -\partial\mathbf{M}_i/\partial\gamma$ , and  $\tilde{\mathbf{L}}_4 = \partial\Phi/\partial\gamma$  in accordance with  $\mathbf{U}_4 \equiv \gamma$ . Since the fourth variable  $\gamma$  is treated on equal footing with the other three variables, all expressions required to compute the matrices  $\mathbf{K}_{i,4}$  and  $\mathbf{N}_{i,4}$  come out of the standard linearization of the problem. This is yet another advantage of including  $\gamma$  as an extra dependent variable.

When dealing with a problem with a volume constraint as in Equation (15b), it is necessary to compute the derivative of the constraint with respect to  $\gamma$

$$\frac{\partial}{\partial\gamma_n} \left[ \frac{1}{|\Omega|} \int_{\Omega} \gamma(\mathbf{r}) \, d\mathbf{r} - \beta \right] = \frac{1}{|\Omega|} \int_{\Omega} \varphi_{n,4}(\mathbf{r}) \, d\mathbf{r} \tag{31}$$

which can be obtained by assembling  $\hat{\mathbf{L}}_4$  with  $\hat{\Gamma}_4 \equiv \mathbf{0}$ ,  $\hat{F}_4 \equiv 1$ , and  $\hat{G}_4 \equiv 0$ . In the appendix we have included a transcript of the code required to set up and solve the example from Section 4.2 below with FEMLAB. It amounts to 111 lines of code, of which the majority are spent on setting up the actual Navier–Stokes flow problem. Only a minor part goes to set up the adjoint problem and perform the sensitivity analysis. Moreover, this part contains almost no reference to the actual physical problem being solved, and therefore it should apply for any multi-field problem expressed in the divergence form Equations (10a)–(10c) with an objective function of the form

of Equation (11). The code example employs, but does not include, a MATLAB implementation of the MMA optimization algorithm [11–13].

*3.5.1. Mesh dependence and regularization techniques.* It is well known that many topology optimization problems have trouble with mesh dependence, e.g. in stiffness design of mechanical structures it often pays to replace a thick beam with two thinner beams for a given amount of material. As the finite element mesh is refined, smaller and smaller features can be resolved and therefore appear in the optimized structure. In that sense the flow problem that we consider here is atypical because it is generally unfavourable to replace a wide channel with two narrower channels; hence the proof for the existence of a unique optimal solution with respect to minimization of the total power dissipation in Reference [6].

The problem with mesh dependence can be overcome by various regularization techniques based on filtering of either the design variable  $\gamma(\mathbf{r})$  or the sensitivity  $d\Phi/d\gamma$  [2]. The regularization works by defining a certain length scale  $r_0$  below which any features in  $\gamma(\mathbf{r})$  or  $d\Phi/d\gamma$  are smeared out by the filter; in both cases this results in optimized structures with a minimal feature size  $\sim r_0$  independent of the mesh refinement. Unfortunately FEMLAB does not come with such a filter, and hence its implementation is an issue that has to be dealt with before our methodology here can be successfully applied to problems that display mesh dependence.

One strategy is to implement the convolution operation of the filter directly [2]. If the computational domain is rectangular and discretized by square finite elements this is both efficient and fairly easy to program, if not one simply uses a standard filter from the MATLAB Image Processing Toolbox. For an unstructured mesh of triangular elements the programming is more involved and slow in MATLAB due to the need to loop over the design variable nodes and searching the mesh for neighbouring nodes within the filter radius. Therefore an explicit matrix representation of the filter would often be preferred [18].

Another possible strategy is to solve an artificial diffusion problem for the design variable  $\gamma(\mathbf{r})$  over some period in ‘time’  $\Delta t = r_0^2/k$  where  $k$  is the ‘diffusion’ constant. The diffusion equation could be included into the fields of Equation (29) that are otherwise unused, and the ‘time’ evolution solved using the built-in timestepper in FEMLAB. This procedure is equivalent to the action of a filter with Gaussian kernel of width  $r_0$ , and it conserves the total amount of material during the filter action. The same approach could be used to smooth out the sensitivity. However, because  $d\Phi/d\gamma_n$  is sensitive to the local element size one would need to rescale it with  $\int_{\Omega} \phi_{4,n}(\mathbf{r}) d\mathbf{r}$  before application of the filter—actually this is true for any filter acting on  $d\Phi/d\gamma$  whenever the mesh is irregular and  $\int_{\Omega} \phi_{4,n}(\mathbf{r}) d\mathbf{r}$  not constant for all  $n$ .

The major disadvantage of this strategy is that it involves solving a time evolution problem in each design iteration which could easily turn out to be the most time-consuming step. Alternatively the timestepping algorithm could be implemented by hand, e.g. deciding on the Crank–Nicholson algorithm with a fixed stepsize  $\delta t \leq \Delta t$ . The mass and stiffness matrices for the diffusion problem can be obtained from FEMLAB, and the corresponding iteration matrix need only be factorized once for the given stepsize and could thus be reused in all subsequent design iterations, making this approach relatively cheap, although more cumbersome than using the built-in timestepper.

*3.5.2. Large-scale problems.* For large-scale problems and three-dimensional modelling it is often necessary to resort to iterative linear solvers because the memory requirements of a direct matrix factorization becomes prohibitive. In that case the strategy we have outlined

here of obtaining the  $\mathbf{K}$  and  $\mathbf{N}$  matrices directly as sparse matrices in MATLAB and simply transposing  $\mathbf{K}$  before the solution of the adjoint problem may not be practical. Alternatively, if the original physical problem is expressed in divergence form then the FEMLAB representation of that problem contains the symbolic derivatives of  $\Gamma_i$ ,  $F_i$ , and  $G_i$  appearing in Equation (26). These fields can be transposed and set in the auxiliary copy of the original problem such that it effectively defines  $\tilde{\mathbf{K}}_{ij} = \mathbf{K}_{ji}^T$ , while retaining the definitions in Equation (29) for the right-hand side vector  $\tilde{\mathbf{L}}_i$ . Then the adjoint problem Equation (23) can be solved *without* direct handling of the matrices in MATLAB, and using the same iterative solver algorithm as would be employed for the original physical problem. Ultimately we still require an explicit representation of the matrices  $\mathbf{K}_{i,4}$  and  $\mathbf{N}_{i,4}$  to evaluate the sensitivity  $d\Phi/d\gamma$  in Equation (30).

From our point of view the major advantage of using FEMLAB in its present stage of development for topology optimization is not in solving large scale problems, though, but rather in the ease of implementation and the ability to handle problems with coupling between several physical processes.

#### 4. NUMERICAL EXAMPLES

In this section we present our results for topology optimization of Navier–Stokes flow for two particular model systems that we have studied. These systems have been chosen because they illustrate the dependence of the solution on the two dimensionless numbers  $Re$  and  $Da$ , measuring the importance of the inertia of the fluid and the permeability of the porous medium, respectively, relative to viscosity. Moreover we discuss the dependence of the solution on the initial condition for the material distribution.

For simplicity and clarity we have chosen to consider only two-dimensional model systems. We note that the dimensionality of the problems has no fundamental consequence for the method and the numerics, but only affects computer memory requirements and the demand for CPU time. Our 2D examples can therefore be viewed as idealized test cases for our implementation of topology optimization. Yet, the 2D models are not entirely of academic interest only as they represent two limits of actual 3D systems. Due to planar process technology many contemporary lab-on-a-chip systems have a flat geometry with typical channel heights of about 10  $\mu\text{m}$  and widths of 1 mm, i.e. an aspect ratio of 1:100 [14]. One limit is the case where the channel width is constant and the channel substrate and lid are patterned with a profile that is translation invariant in the transverse (width) direction. In the limit of infinitely wide channels the 2D-flow in the plane perpendicular to the width-direction is an exact solution, while it remains an excellent approximation in a 1:100 aspect ratio channel. This is the model system we have adopted for the numerical examples in the present work. The other important limit is when the channel width is not constant, but the channel height is sufficiently slowly varying that the vertical component of the fluid velocity can be neglected. Then writing the Navier–Stokes equation for the velocity averaged in the vertical (height) direction, the out-of-plane shear imposed by the channel substrate and lid gives rise to an absorption term  $-\alpha\mathbf{v}$ . This approach was studied by Borrvall and Petersson [6], see also the footnote in Section 2.1. Thus, if one is interested in optimizing the height-averaged flow field in a flat channel the 2D model is sufficient.

When solving the Navier–Stokes flow problem we use the standard direct linear solver in FEMLAB in the Newton iterations. Typically we have around 6000 elements in the mesh,

corresponding to 30 000 degrees-of-freedom. The constrained optimization problem is solved using a MATLAB implementation of the MMA algorithm kindly provided by Svanberg [11, 13], except that we modified the code to use the globally convergent scheme described in Reference [12]. The example script included in the appendix employs only the basic algorithm `mmasub`, though. The design iterations are stopped when the maximal change in the design field is  $\|\gamma^{(k+1)} - \gamma^{(k)}\|_\infty \leq 0.01$ , at which point we typically have  $|\Phi^{(k+1)} - \Phi^{(k)}| < 10^{-5}$ .

#### 4.1. Example: a channel with reverse flow

Our first numerical example deals with the design of a structure that at a particular point inside a long straight channel can guide the flow in the opposite direction of the applied pressure drop. The corresponding problem with a prescribed flow rate was first suggested and investigated by Gersborg-Hansen [8]. We elaborate on it here to illustrate the importance of the choice of permeability for the porous medium.

The computational domain is shown in Figure 1. It consists of a long straight channel of height  $\ell$  and length  $L = 10\ell$ ; the actual design domain, inside which the porous material is distributed, is limited to the central part of length  $5\ell$ . The boundary conditions prescribe a pressure drop of  $\Delta p$  from the inlet (left) to the outlet (right), and no-slip for the fluid on the channel side walls.

The optimization problem is stated as a minimization of the horizontal fluid velocity at the point  $\mathbf{r}^*$  at the centre of the channel, i.e. the design objective is

$$\Phi = v_1(\mathbf{r}^*) \quad (32)$$

In terms of the general objective Equation (11) this is obtained with  $A \equiv v_1(\mathbf{r})\delta(\mathbf{r} - \mathbf{r}^*)$  and  $B \equiv 0$ . There is no explicit need for a volume constraint because neither of the extreme solutions of completely filled or empty can be optimal. When the design domain is completely filled with porous material we expect a flat flow profile with magnitude below  $\Delta p / (5\ell\alpha_{\max})$ . In the other extreme case when the channel is completely devoid of porous material the solution is simply a parabolic Poiseuille profile with maximum

$$v_0 = \frac{\ell^2 \Delta p}{8\eta L} \quad (33)$$

However, a structure that *reverses* the flow such that  $v_1(\mathbf{r}^*)$  becomes negative will be superior to both these extreme cases in the sense of minimizing  $\Phi$ .

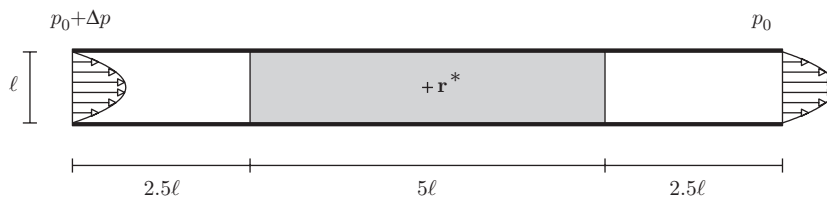


Figure 1. Computational domain for the reverse flow example. The design domain (grey) has length  $5\ell$  and height  $\ell$ , and the fluid enters and leaves the design domain through leads of length  $2.5\ell$ . The boundary conditions prescribe a pressure drop of  $\Delta p$  across the system, and the design objective is to reverse the flow direction at the point  $\mathbf{r}^*$  at centre of the channel.

*4.1.1. Reverse flow in the Stokes limit,  $Re=0$ .* We first consider the Stokes flow limit of small  $\Delta p$  where the inertial term becomes negligible. The problem is then linear and the solution is characterized by a single dimensionless parameter, namely the Darcy number  $Da$ , Equation (6). We have solved the topology optimization problem for different values of  $Da$ . The initial condition for the material distribution was  $\gamma^{(0)} = 1$ , and the parameter  $q$  determining the shape of  $\alpha(\gamma)$  in Equation (4) was set to  $q=0.1$ . Anticipating that the structural details close to  $\mathbf{r}^*$  should be more important than those further away we chose a non-uniform finite element mesh with increased resolution around  $\mathbf{r}^*$ .

Figure 2 shows the optimal structures obtained for  $Da = 10^{-3}$ ,  $10^{-4}$ ,  $10^{-5}$  and  $10^{-6}$ . They all consist of two barriers defining an  $S$ -shaped channel that guides the fluid in the reverse direction of the applied pressure drop. At  $Da = 10^{-3}$  the two barriers are rather thick but leaky with almost all the streamlines penetrating them; as the Darcy number is decreased the optimal structures become thinner and less penetrable. This result can be interpreted as a trade-off between having either thick barriers or wide channels. Thick barriers are necessary to force the fluid into the  $S$ -turn, while at the same time the open channel should be as wide as possible in order to minimize the hydraulic resistance and maximize the fluid flow at the prescribed pressure drop.

Notice that if we had chosen to prescribe the flow rate through the device rather than the pressure drop, then the optimal solution would have been somewhat different. When the flow rate is prescribed, it pays to make the gap between the barriers very small and the barriers very thick in order to force the fixed amount of fluid flow through the narrow contraction. The optimal structure is therefore one with a very large hydraulic resistance. In Reference [8], this problem was circumvented by adding a constraint on the maximal power dissipation allowed at the given flow rate.

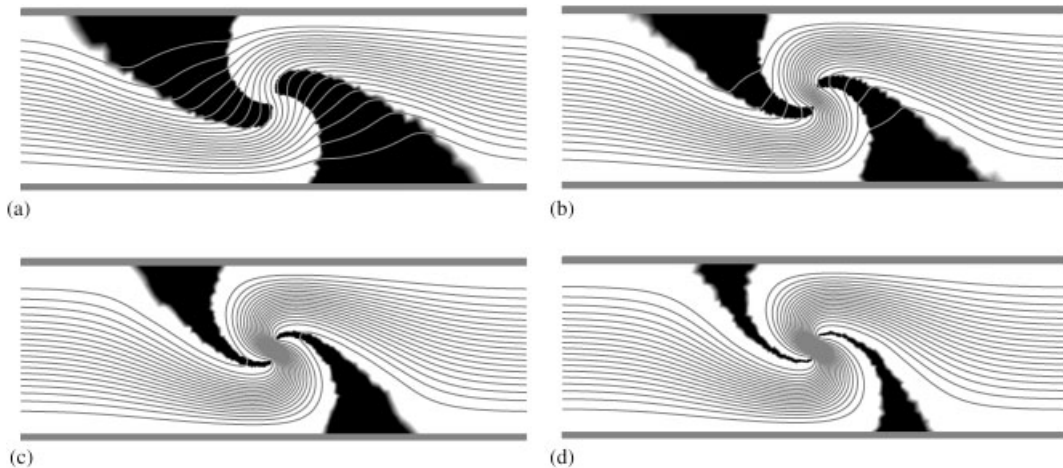


Figure 2. Optimized structures (black) and streamlines at 5% intervals for Stokes flow ( $Re=0$ ) at Darcy numbers decreasing from  $10^{-3}$  to  $10^{-6}$ . Only the central part of length  $3\ell$  of the design domain is shown. The structures consist of two barriers defining an  $S$ -shaped channel that reverses the flow at the central point  $\mathbf{r}^*$ . As the Darcy number is decreased, the optimized structures become thinner and less permeable: (a)  $Da=10^{-3}$ ; (b)  $Da=10^{-4}$ ; (c)  $Da=10^{-5}$ ; and (d)  $Da=10^{-6}$ .

In order to validate the optimality of the structures computed by the topology optimization we do as follows: For each of the optimized structures from Figure 2 we freeze the material distribution and solve the flow problem for a range of Darcy numbers. The resulting family of curves for  $v_1(\mathbf{r}^*)$  vs  $Da$  is shown in Figure 3 where it is seen that each of the four structures from Figure 2 do indeed perform better in minimizing  $v_1(\mathbf{r}^*)$  than the others at the value of  $Da$  for which they are optimized.

For  $Da \lesssim 10^{-5}$  the optimal value of  $v_1(\mathbf{r}^*)$  tends to saturate because the thin barriers are then almost completely impermeable and the open channel cannot get much wider. In this limit the thickness of the optimized barrier structures approach the mesh resolution as seen in Figure 2(d). When the optimal barrier thickness gets below the mesh size we have observed the appearance of artificial local optima for the barrier structure. The problem is that the thin barriers cannot continuously deform into another position without going through an intermediate structure with barriers that are thicker by at least one mesh element. Depending on the initial condition, the optimization algorithm can therefore end up with a sub-optimal structure. We have tried to work around this problem by decreasing the value of  $q$  in order to smear out the solid/void interfaces and thus reduce the cost of going through the intermediate structure. This did not work out well; the reason may be that the smearing property of a convex  $\alpha(\gamma)$  was derived for the objective of minimizing the power dissipation subject to a volume constraint. In the present example we are dealing with a different objective and have no volume constraint. However, when the barrier structures are resolved with at least a few elements across them the artificial local optima tend to be insignificant. Thus the problem can be avoided by choosing a sufficiently fine mesh, or by adaptively refining the mesh at the solid/void interfaces.

Returning to Figure 3 we notice that as  $Da$  increases all the structures perform poorly in minimizing  $v_1(\mathbf{r}^*)$ , as they all approach  $v_0$ . Extrapolating this trend one might suspect that the  $S$ -turn topology will cease to be optimal somewhere above  $Da = 10^{-3}$  simply because the

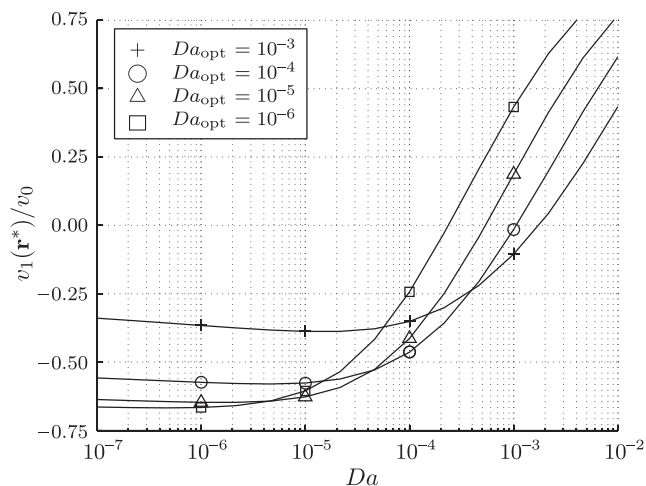


Figure 3. Comparing the performance of the structures from Figure 2 optimized at  $Da_{\text{opt}}$  for different values of  $Da$ . The objective  $v_1(\mathbf{r}^*)$  is normalized with the velocity in an empty channel,  $v_0$ , c.f. Equation (33).

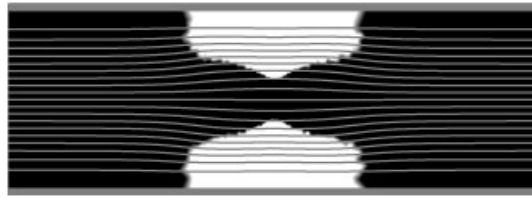


Figure 4. Optimized structure (black) and streamlines for Stokes flow at  $Da = 10^{-2}$ ; only the central part of length  $3\ell$ . The design domain is completely filled with porous material, except immediately above and below  $\mathbf{r}^*$  where two empty regions emerge. These voids divert the flow away from  $\mathbf{r}^*$ , resulting in a low velocity  $v_1(\mathbf{r}^*) = 0.1v_0$ .

porous material becomes too permeable to make reversal of the flow direction possible. We have tested this hypothesis by performing an optimization at  $Da = 10^{-2}$ , resulting in the structure shown in Figure 4 where the value of the objective is  $v_1(\mathbf{r}^*) = 0.1v_0$ . It is seen to display a different topology from those of Figure 2, with the design domain is almost completely filled with porous material blocking the flow through the channel. Only immediately above and below the point  $\mathbf{r}^*$  we see two empty regions emerging that act to guide the flow away from  $\mathbf{r}^*$ .

Actually, in all four cases from Figure 2, starting from an empty channel the design iterations initially converge towards a symmetric structure blocking the flow like that in Figure 4. However, at a certain point in the iterations an asymmetry in the horizontal plane is excited and the structure quickly changes to the two-barrier *S*-geometry. Whether the optimization converge to an *S*- or an inverted *S*-turn depends on how the asymmetry is excited from numerical noise or irregularity in the finite element mesh; in fact the structure in Figure 2(b) originally came out as an inverted *S* but was mirrored by hand before plotting it to facilitate comparison with the three other structures.

**4.1.2. Reverse flow at finite Reynolds number.** We now consider flow at finite Reynolds number, characterized by the two dimensionless numbers  $Re$  and  $Da$ . The geometry and boundary conditions remain unchanged, for convenience we introduce a non-dimensional pressure drop  $\Delta\tilde{p} = \Delta p \rho \ell^2 / \eta^2$ , and finally we fix the Darcy number at  $Da = 10^{-5}$ . We note from Figure 2 that this Darcy number allows some but not much fluid to penetrate the walls. We have nevertheless chosen this Darcy number for practical reasons, as the walls are ‘solid’ enough and a lower value (more ‘solid’ wall) would increase the calculation time.

We have solved the topology optimization problem for different values of  $\Delta\tilde{p}$ , always using an empty channel as initial condition. The results are shown in Figures 5(a)–(c) for  $\Delta\tilde{p} = 0.2, 0.5$ , and  $1.0 \times 10^5$ , where only a few streamlines are seen to penetrate the barriers. For comparison we also consider the flow field obtained when the structure optimized for Stokes flow at  $Da = 10^{-5}$  is frozen and exposed to the three different elevated pressure drops. This is shown in Figures 5(d)–(f): As the pressure drop is increased, more and more streamlines penetrate the barriers. Moreover, we find a recirculation region emerging behind the second barrier which reduces the pressure drop over the neck between the barriers.

Returning to Figures 5(a)–(c), we find that the structures that have been optimized for the corresponding pressure drops are generally thicker than that optimized for Stokes flow, which reduces the number of streamlines penetrating them. Also a beak-like tip grows on the second

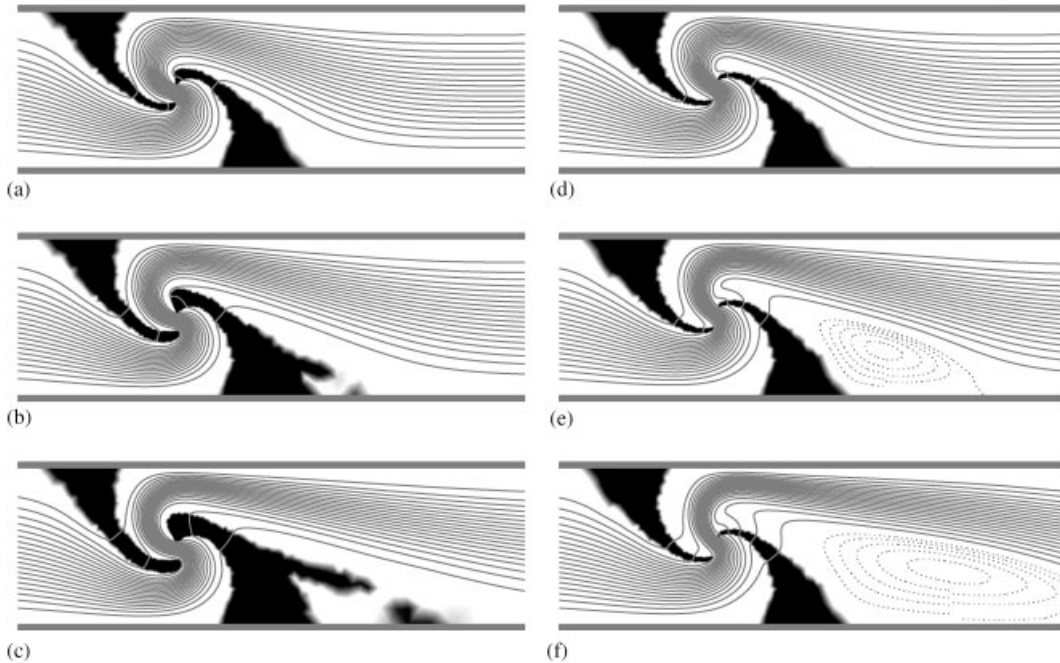


Figure 5. Optimized structures (black) and streamlines for Navier–Stokes flow; only a part of length  $3.25\ell$  near the centre of the channel is shown. Panels (a)–(c) to the left show the optimized structures for different values of the control parameter  $\Delta\tilde{p} = \Delta p \rho \ell^2 / \eta^2$ . For comparison the flow field when the optimized structure from Figure 2(c) is frozen and exposed to the elevated pressure drops is shown in panels (d)–(f) to the right. The Reynolds number is defined as  $Re = \rho \ell v_{\max} / \eta$  where  $v_{\max}$  is the maximal velocity measured at the inlet; note that for a particular value of  $\Delta\tilde{p}$ , the Reynolds number is not fixed but differs slightly between left and right column: (a)  $\Delta\tilde{p} = 0.2 \times 10^5$  [ $Re = 23$ ]; (b)  $\Delta\tilde{p} = 0.5 \times 10^5$  [ $Re = 42$ ]; (c)  $\Delta\tilde{p} = 1.0 \times 10^5$  [ $Re = 64$ ]; (d)  $\Delta\tilde{p} = 0.2 \times 10^5$  [ $Re = 26$ ]; (e)  $\Delta\tilde{p} = 0.5 \times 10^5$  [ $Re = 47$ ]; and (f)  $\Delta\tilde{p} = 1.0 \times 10^5$  [ $Re = 71$ ].

barrier that acts to bend the fluid stream down. Finally, on the back of the second barrier a wing- or spoiler-like structure appears that removes the recirculation.

In summary, our first example has demonstrated that our implementation of topology optimization works, but that the optimal design and performance may depend strongly on the choice of the Darcy number. In particular, the zero  $Da$  limit solution contains zero thickness and yet impermeable barriers deflecting the fluid. In order to approximate this solution at finite  $Da$  and on a finite resolution mesh it is important to choose the Darcy number small enough that even thin barriers can be almost impermeable, but large enough to avoid difficulties with artificial local optima in the discretized problem when the barrier thickness decreases below the mesh resolution.

#### 4.2. Example: a four-terminal device

Our second numerical example deals with minimization of the power dissipation in a four-terminal device subject to a volume constraint. The problem is found to exhibit a discrete

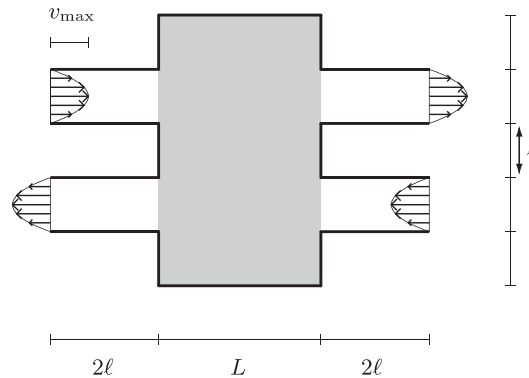


Figure 6. Schematic illustration of the four-terminal device. Two inlet and two outlet leads (white areas) of height  $\ell$  and length  $2\ell$  are attached to the design domain (grey) of height  $5\ell$  and length  $L$ . The flow is characterized by the Reynolds number  $Re = \rho\ell v_{\max}/\eta$ , where  $v_{\max}$  is the maximal velocity at the inlets.

change in optimal topology driven by the inertial term. The four-terminal device is related to one considered by Borrvall and Petersson for Stokes flow in Reference [6]; the present example demonstrates that the optimization algorithm has difficulties in finding the optimal topology when there are two strong candidates for the global optimum.

The computational domain, shown in Figure 6, consists of a rectangular design domain (grey) to which two inlet and two outlet leads (white) are attached symmetrically. The boundary conditions prescribe parabolic profiles for the flow at the inlets, zero pressure and normal flow at the outlets, and no-slip on all other external boundaries. Choosing the height  $\ell$  of the leads as our characteristic length scale, we define the Reynolds number as  $Re = \rho\ell v_{\max}/\eta$ , where  $v_{\max}$  is the maximal velocity at the inlets. The Darcy number is fixed at  $Da = 10^{-4}$  to obtain reasonably small leakage through the porous walls.

The optimization problem is stated as a minimization of the total power dissipation inside the computational domain, given by Equation (7a), subject to the constraint that at most a fraction  $\beta = 0.4$  of the design domain should be without porous material, c.f. Equation (15b).

Figures 7(a) and (b) shows the two optimal structures obtained for  $Re = 20$  and  $200$ , respectively, in a geometry with  $L = 3.5\ell$ . At  $Re = 20$  the optimal structure turns out to be a pair of  $U$ -turns connecting the inlets to the outlets on the same side of the design domain, while at  $Re = 200$  the optimal structure is a pair of parallel channels. In order to minimize the power dissipation at low  $Re$ , the channel segments should be as short and as wide as possible, which favours the  $U$ -turns in Figure 7(a). However, as the Reynolds number is increased, the cost of bending the fluid stream grows. When inertia dominates, larger velocity gradients appear in the long ‘outer lane’ of the  $U$ -turn. This increases the dissipation compared to low  $Re$ , where more fluid flows in the shorter ‘inner lane’. At a certain point it will exceed the dissipation in the parallel channels solution

$$\Phi_0 = \frac{96}{9} \left( 4 + \frac{L}{\ell} \right) \eta v_{\max}^2 \tag{34}$$

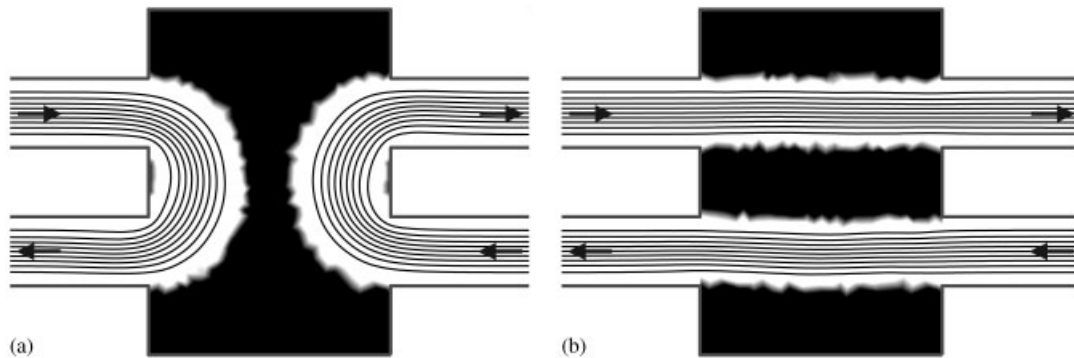


Figure 7. Optimal structures (black) and streamlines at 10% intervals for the four-terminal device at Reynolds number  $Re = 20$  and  $200$ , respectively, in a geometry with  $L = 3.5\ell$ : (a)  $Re = 20$ ; and (b)  $Re = 200$ .

as estimated from Poiseuille flow in two straight channels, each of length  $L + 4\ell$  and height  $\ell$ . This number is independent of inertia due to translation symmetry, and we use  $\Phi_0$  as a natural unit of power dissipation (per unit length in the third dimension) in the following.

Clearly the Reynolds number at which the transition between the two classes of solutions occurs will depend strongly on the ratio  $L/\ell$ . For short lengths  $L \lesssim 2\ell$  the parallel channels solution is expected to be optimal at all  $Re$ , whereas for long lengths  $L \gtrsim 3\ell$  the  $U$ -turn solution should be significantly better than the parallel channels solution at low  $Re$ .

**4.2.1. Dependence on the Reynolds number.** In the following we investigate more closely the transition between the  $U$ -turns and the parallel channels solution as a function of the Reynolds number for the particular geometry  $L = 3\ell$ . The topology optimization problem is solved for different  $Re$  in the range  $0$ – $200$ , using a homogeneous material distribution  $\gamma^{(0)} = 0.4$  as initial condition. For the parameter  $q$  determining the shape of  $\alpha(\gamma)$  in Equation (4) we use a two-step solution procedure as suggested in Reference [1]. First the problem is solved with  $q = 0.01$  in order to obtain a solution with slightly smeared-out solid/void interfaces. Next this material distribution is used as initial guess for an optimization with  $q = 0.1$  which generates fully discrete solid/void interfaces at the resolution of our finite element mesh.

Figure 8(a) shows the result for the normalized power dissipation  $\Phi/\Phi_0$  obtained as a function of  $Re$ . At low Reynolds numbers the optimized solutions correctly come out as  $U$ -turns with a power dissipation  $\Phi$  that is clearly less than  $\Phi_0$ . However, at high Reynolds numbers  $Re > 90$  the method fails because the optimized solutions continue to come out as  $U$ -turns even though this yields  $\Phi/\Phi_0 > 1$ . For  $Re \geq 160$  the solution jumps from the simple  $U$ -turns to a hybrid structure, as shown in the inset. The full lines in Figure 8(a) show the result when the material distributions optimized for  $Re = 0$ ,  $50$ , and  $180$ , respectively, are frozen and the power dissipation evaluated at different  $Re$ . It is seen that the optimized solutions, marked ( $\circ$ ), all fall on or below the full lines which confirms that they are indeed superior to the other solutions of the  $U$ -turn family. This also holds for  $Re > 90$ , except for the hybrid structures at  $Re \geq 160$ , that are actually inferior to the  $U$ -turns. Moreover, at  $Re = 160$  the optimized solution falls slightly above that optimized at  $Re = 180$ . This could be an indication

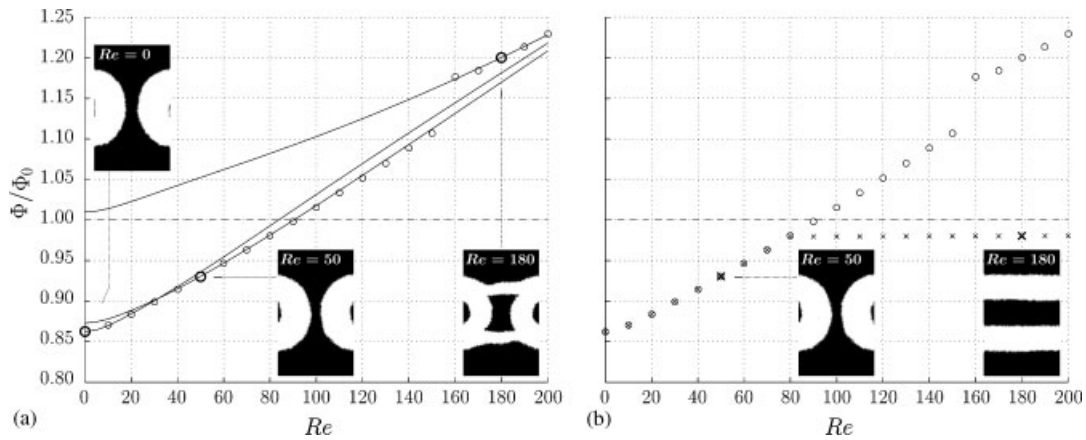


Figure 8. Power dissipation  $\Phi$  in structures optimized for different Reynolds numbers; normalized with the Poiseuille flow result  $\Phi_0$  (dashed line): (a) markers ( $\circ$ ) show results when  $\gamma^{(0)} = 0.4$  is used as initial condition, failing to find the optimal solution for  $Re > 90$ . Full lines show the performance of the structures optimized at  $Re = 0, 50$ , and  $180$ , when evaluated at different Reynolds numbers. As expected, all points fall on or below the full lines, except the hybrid solutions for  $Re \geq 160$ ; and (b) comparison between the two different initial conditions  $\gamma^{(0)} = 0.4$  ( $\circ$ ) and  $\gamma^{(0)} = 1$  ( $\times$ ), showing the success of the empty channel initial condition in finding the optimal solution. The crosses ( $\times$ ) fall slightly below  $\Phi/\Phi_0 = 1$  due to leakage through the porous walls (see the text).

that the hybrid structures are not local optima in design space after all, but rather a very narrow saddle point that the optimization algorithm has a hard time getting away from.

The difficulty is that the two families of solutions, the  $U$ -turns and the parallel channels, are both deep local minima for the power dissipation in design space. Using  $\gamma^{(0)} = 0.4$  as initial condition, the initial permeability is everywhere very low, such that the porous friction almost completely dominates the inertia and viscous friction in the fluid. Therefore the iteration path in design space is biased towards low Reynolds numbers and the  $U$ -turns solution.

In order to circumvent this problem we have tried using a completely empty design domain with  $\gamma^{(0)} = 1$  as initial condition. This should remove the bias towards the  $U$ -turns and allow the optimization algorithm to take inertia into account from iteration one. The result is shown in Figure 8(b). For  $Re \leq 80$  the solutions are still  $U$ -turns, whereas for  $Re \geq 90$  they come out as parallel channels. Notice that  $\Phi/\Phi_0$  for the parallel channels solution is actually slightly less than unity, namely 0.98. This is due to a small amount of fluid seeping through the porous walls defining the device, which lowers the hydraulic resistance compared to the Poiseuille flow result derived for solid walls.<sup>||</sup>

Strictly speaking the initial condition  $\gamma^{(0)} = 1$  is not a feasible solution because it violates the volume constraint that at least a fraction  $1 - \beta = 0.6$  of the design domain should be filled

<sup>||</sup>The flow in a straight channel of height  $\ell$  bounded by two porous walls of thickness  $\ell$  can easily be found analytically. At  $Da = 10^{-4}$  the hydraulic resistance of this system is 94% of that for a channel of height  $\ell$  bounded by solid walls, and it approaches this zero  $Da$  limit only as  $\sqrt{Da}$ . When  $L = 3\ell$  we therefore expect a power dissipation  $\Phi/\Phi_0 = (3 \times 0.94 + 4)/7 = 0.97$  for the parallel channels solution, including the leads. This is close to the observed 0.98.

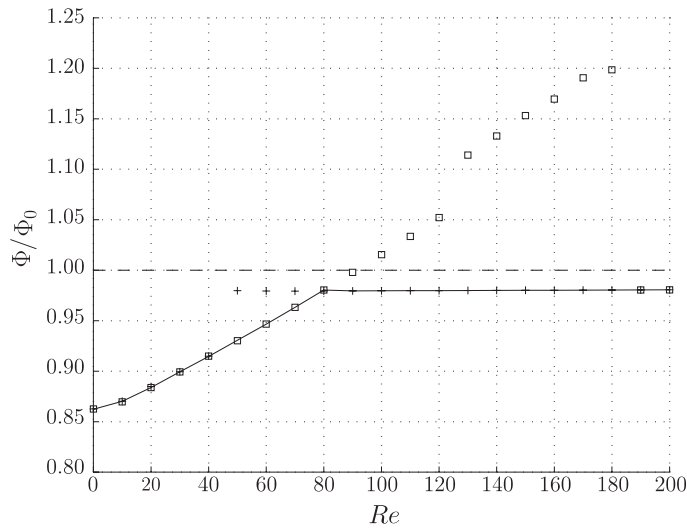


Figure 9. Comparison between structures optimized with the initially non-feasible material distribution  $\gamma^{(0)} = 1$  for different penalty parameters in the MMA optimization algorithm, revealing the difficulty in choosing the condition for finding the global optimum. Full line: the successful result from Figure 8(b) with moderate penalty; (+) lower penalty yielding wrong result for  $40 < Re < 80$ ; (□) higher penalty yielding wrong results for  $80 < Re < 190$ .

with porous material. However, the MMA optimization algorithm penalizes this and reaches a feasible solution after a few iterations. This is controlled by choosing a penalty parameter. If the penalty for violating the constraint is small, the material is added slowly and only where it does not disturb the flow much. If the penalty is large, the material is added quickly and almost homogeneously until the constraint is satisfied. The successful result from Figure 8(b) was obtained with a moderate penalty. In Figure 9 this is compared with results for smaller and larger penalty parameters, respectively. The figure shows that with the small penalization, the solution jumps to the parallel channels already at  $Re = 50$  which is not optimal. For the large penalization, the solution does not jump until  $Re \geq 190$ . Also we observe hybrid structures similar to those in Figure 8(a) for  $Re \geq 130$ . We have thus not full control over the convergence towards the global optimum.

**4.2.2. Discussion of problems with local optima.** Further insight into the problem of local versus global optima is gained by inspecting the flow field in the initial material distribution  $\gamma^{(0)}$ . This is shown in Figure 10 for the Stokes flow limit,  $Re = 0$ . The streamlines are drawn as 10% contours of the streamfunction, and Figure 10(a) shows that for  $\gamma^{(0)} = 0.4$  the streamline density is largest between the two leads on the same side of the design domain. Based on the sensitivity  $d\Phi/d\gamma$  the optimization algorithm therefore decides to remove material from these strong-flow regions in order to reduce the porous friction. The iteration path in design space is therefore biased towards the *U*-turn solution. This remains true even at finite Reynolds numbers as long as the porous friction initially dominates inertia.

Figure 10(b) shows that when  $\gamma^{(0)} = 1$  the streamline density is largest between the leads on the opposite side of the design domain. Because the volume constraint is violated the

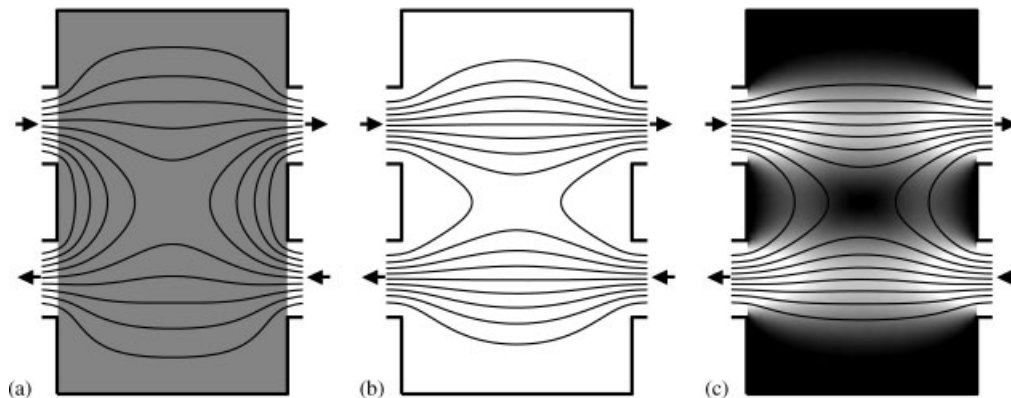


Figure 10. Flow distributions at  $Re=0$ ,  $L=3\ell$  and  $q=0.01$ : (a) initial design field  $\gamma^{(0)}=0.4$ ; (b) initial design field  $\gamma^{(0)}=0.4$ ; and (c) the optimal design field  $\gamma^{(*)}$  obtained at  $Da=10^{-2}$ .

optimization algorithm has to place material somewhere, which it does in the weak-flow regions. The solution is therefore biased towards the parallel channels. Indeed if the penalty is chosen very small, the optimized solution comes out as parallel channels even for Stokes flow at  $L=3\ell$ , which is far from optimal. When the penalty is larger and the material is added faster, we move away from this adiabatic solution and closer to the situation for  $\gamma^{(0)}=0.4$ .

The additional complexity associated with making a proper choice of the penalty parameter is somewhat inconvenient. We have therefore attempted to construct a more convex problem by increasing the initial permeability. This can be done either by increasing the Darcy number, or by decreasing the parameter  $q$ , c.f. Equation (4). Figure 10(c) shows the optimal solution  $\gamma^{(*)}$  obtained for  $Da=10^{-2}$  and  $q=0.01$  at  $Re=0$ . At this level the problem is convex because the solution is independent of the initial condition. Using this material distribution as initial guess and gradually decreasing the permeability to  $Da=10^{-4}$  and  $q=0.1$  we correctly end up in the  $U$ -turn solution. However, it is evident from Figure 10(c) that  $\gamma^{(*)}$  has a fair amount of parallel channels nature. Using the same procedure of gradually decreasing the permeability at higher Reynolds numbers therefore result in a transition to the parallel channels solution already for  $Re \geq 30$ , which is not optimal. Moreover, when the Reynolds number is increased and the inertia starts to play in, the system tends to loose convexity even at the initial high permeability.

In summary, the topology optimization has difficulties in finding the global optimum for the problem. There are two strong candidates for the optimal structure, and the solution found is sensitive to the initial condition for the material distribution. Using an empty channel as initial condition, the method is able to find the correct solution for all Reynolds numbers. However, this successful result depends on a particular choice of the penalty parameter in the MMA algorithm. By using a high initial permeability of the porous medium, it is possible to convexify the problem at low Reynolds numbers, but continuation of this solution to the desired low permeability does not generally lead to the global minimum of the non-convex problem.

In the original paper Reference [6] it was argued that in Stokes flow the true optimal design should be rather insensitive to the choice of the Darcy number, although the dissipated power

may deviate quite a lot from the zero  $Da$  limit. In our work we have observed that the actual solution found by the topology optimization may depend a great deal on the choice of the Darcy number, whereas the dissipated power should approach the zero  $Da$  limit roughly as  $\sqrt{Da}$ .

## 5. CONCLUSION

Based on the work of Borrvall and Petersson [6] we have extended the topology optimization of fluid networks to cover the full incompressible Navier–Stokes equations in steady-state. Our implementation of the method is based on the commercial finite element package FEMLAB, which reduces the programming effort required to a minimum. Formulating the problem in terms of a general integral-type objective function and expressing the governing equations in divergence form makes the implementation very compact and transparent. Moreover, the code for performing the sensitivity analysis should remain almost the same for any problem expressed in this way, whereas that required for describing the physical problem of course changes. Topology optimization of multi-field problems can therefore be dealt with almost as easy as a single realization of the underlying physical problem.

We would like to mention that our methodology is not as such restricted to the (large) class of physical problems that can be expressed in divergence form. FEMLAB also allows problems to be stated directly in weak form, e.g. for systems with dynamics at the boundaries. This does in fact not invalidate the sensitivity analysis worked out in Section 3.4, since this analysis only relies on the basic structure of the discretized non-linear problem and the availability of the Jacobian matrix. It is therefore possible to apply our methodology to even larger classes of physical problems than the ones comprised by the divergence form.

Our implementation of topology optimization has been tested on two fluidics examples in 2D, both illustrating the influence of different quantities and conditions on the efficiency of the optimization method.

The first example, a channel with reversed flow, illustrates the influence of the Reynolds number  $Re$  and the Darcy number  $Da$  on the solutions. We have shown that the choice of  $Da$  has a strong impact on the solution when the structure contains barriers to deflect the fluid stream.

The second example, minimization of the power dissipation in a four-terminal device, reveals the problems of determining the global minimum when two strong minima are competing. This problem is highly non-convex, and we have shown that the solution depends on the initial condition. For an initial homogeneous material distribution, the porous friction dominates and the solution does not come out as the global optimum in all cases. Using an empty channel as the initial state, inertia plays a role from the beginning, and better results can be obtained. However, this initial condition in fact violates the volume constraint, and the part of the optimization routine correcting this depends on a penalty factor. Unfortunately, the particular value chosen for this factor strongly influences the results. Increasing the Darcy number makes the problem more convex, but continuation from large to small  $Da$ , i.e. from high to low permeability of the porous material, does not generally end up in the global optimum.

In conclusion, we have shown that our implementation of topology optimization is a useful tool for designing fluidic devices.

## APPENDIX

```

% FEMLAB CODE FOR THE 4-TERMINAL DEVICE EXAMPLE OF SECTION 4.2
clear fem femadj
% DEFINE REYNOLDS NUMBER, DARCY NUMBER, LENGTH OF DESIGN DOMAIN, AND VOLUME FRACTION
Re = 50;
Da = 1e-4;
L0 = 3.0;
beta = 0.4;
% DEFINE GEOMETRY, MESH, AND SUBDOMAIN/BOUNDARY GROUPS [SEE FIGURE 6]
fem.geom = rect2(0,L0,0,5) + rect2(-2,0,1,2) + rect2(-2,0,3,4) + rect2(L0,L0+2,1,2) ...
+ rect2(L0,L0+2,3,4);
fem.mesh = meshinit(fem,'Hmaxsub',[3 0.125]);
% subdomain groups 1:design domain 2:inlet/outlet leads
fem.equ.ind = {[3] [1 2 4 5]};
% boundary groups 1:walls 2:inlets 3:outlets 4:interior
fem.bnd.ind = {[2:3 5:8 10 12:14 16:18 20:22] [4 23] [1 24] [9 11 15 19]};
% DEFINE SPACE CO-ORDINATES, DEPENDENT VARIABLES, AND SHAPE FUNCTIONS
fem.sdim = {'x' 'y'};
fem.dim = {'u' 'v' 'p' 'gamma'};
fem.shape = [2 2 1 1];
% DEFINE CONSTANTS
fem.const.rho = 1;
fem.const.eta = 1;
fem.const.umax = Re;
fem.const.alphamin = 0;
fem.const.alphamax = 1/Da;
fem.const.q = 0.1;
Phi0 = 96*fem.const.eta*(L0+4)*fem.const.umax^2/9;
% DEFINE EXPRESSIONS ON SUBDOMAIN AND BOUNDARY GROUPS
fem.equ.expr = {'A' 'eta*(2*ux*ux+2*vy*vy+(uy+vx)*(uy+vx))+alpha*(u*u+v*v)' ...
'alpha' {'alphamin+(alphamax-alphamin)*q*(1-gamma)/(q+gamma)' '0'}};
fem.bnd.expr = {'B' '0'};

% DEFINE GOVERNING EQUATIONS AND INITIAL CONDITIONS [SEE EQUATIONS (8) AND (9)]
fem.form = 'general';
fem.equ.shape = {[1:4] [1:3]}; % only define gamma on subdomain group 1
fem.equ.ga = {'-p+2*eta*ux' 'eta*(uy+vx)' {'eta*(uy+vx)' '-p+2*eta*vy'} {0 0} {0 0}};
fem.equ.f = {'rho*(u*ux+v*uy)+alpha*u' 'rho*(u*vx+v*vy)+alpha*v' 'ux+vy' 1};
fem.equ.init = {[0 0 0 beta]};
% DEFINE BOUNDARY CONDITIONS
fem.bnd.shape = {[1:3]}; % do not define gamma on any boundaries
fem.bnd.r = {'u' 'v' 0 0} ... % walls: no-slip
{'u*nx+4*umax*s*(1-s)' 'v' 0 0} ... % inlets: parabolic profile
{0 'v' 0 0} ... % outlets: normal flow
{0 0 0 0}; % interior: nothing
fem.bnd.g = {[0 0 0 0]}; % zero prescribed external forces everywhere
% PERFORM LINEARIZATION, DEGREE-OF-FREEDOM ASSIGNMENT, AND ASSEMBLE INITIAL CONDITION
fem = femdiff(fem);
fem.xmesh = meshextend(fem);
fem.sol = asseminit(fem);

% DEFINE STRUCTURE FOR COMPUTING RIGHT-HAND-SIDE IN ADJOINT PROBLEM [SEE EQUATION (29)]
femadj = fem;
femadj.equ.ga = {'diff(A,ux)' 'diff(A,uy)' {'diff(A,vx)' 'diff(A,vy)' ...
'diff(A,px)' 'diff(A,py)'} {'diff(A,gammax)' 'diff(A,gammay)'};
femadj.equ.f = {'diff(A,u)' 'diff(A,v)' 'diff(A,p)' 'diff(A,gamma)'};
femadj.bnd.g = {'diff(B,u)' 'diff(B,v)' 'diff(B,p)' 'diff(B,gamma)'};
femadj.xmesh = meshextend(femadj);
% GET INDICES OF DESIGN VARIABLE IN THE GLOBAL SOLUTION VECTOR (fem.sol.u)
i4 = find(asseminit(fem,'Init',{'gamma' 1},'Out','U'));
% COMPUTE VOLUME BELOW DESIGN VARIABLE BASIS FUNCTIONS
L = assemble(fem,'Out',{L'});
Vgamma = L(i4);
Vdomain = sum(Vgamma);
% GET INDICES OF VELOCITY-PRESSURE VARIABLES
i123 = find(asseminit(fem,'Init',{'u' 1 'v' 1 'p' 1},'Out','U'));

% DEFINE VARIABLES AND PARAMETERS FOR MMA OPTIMIZATION ALGORITHM [SEE REFERENCES [11,12,13]]
a0 = 1;
a = 0;
c = 20;
d = 0;
xmin = 0;
xmax = 1;
xold = fem.sol.u(i4);
xolder = xold;

```

```

low = 0;
upp = 1;

% DESIGN LOOP FOR THE ACTUAL TOPOLOGY OPTIMIZATION
for iter = 1:100
    % SOLVE NAVIER-STOKES FLOW PROBLEM TO UPDATE VELOCITY AND PRESSURE
    fem.sol = femnlin(fem,'Solcomp',{ 'u' 'v' 'p' }, 'U', fem.sol.u);
    % SOLVE ADJOINT PROBLEM FOR LAGRANGE MULTIPLIERS
    [K N] = assemble(fem,'Out',{ 'K' 'N' }, 'U', fem.sol.u);
    [L M] = assemble(femadj,'Out',{ 'L' 'M' }, 'U', fem.sol.u);
    femadj.sol = femlin('In',{ 'K' K(i123,i123) 'L' L(i123) 'M' zeros(size(M)) 'N' N(:,i123)});
    % SENSITIVITY ANALYSIS
    gamma = fem.sol.u(i4);
    Phi = postint(fem,'A','Edim',2) + postint(fem,'B','Edim',1);
    dPhidgamma = L(i4) - K(i123,i4)*femadj.sol.u;
    % PERFORM MMA STEP TO UPDATE DESIGN FIELD
    x = gamma;
    f = Phi/Phi0;          g = gamma'*Vgamma/Vdomain - beta;
    dfdx = dPhidgamma/Phi0;    dgdx = Vgamma/Vdomain;
    d2fdx2 = zeros(size(gamma)); d2gdx2 = zeros(size(gamma));
    [xnew,y,z,lambda,ksi,eta,mu,zeta,s,low,upp] = mmasub(1,length(gamma),iter, ...
        x,xmin,xmax,xold,xolder,f,dfdx,d2fdx2,g,dgdx,d2gdx2,low,upp,a0,a,c,d);
    xolder = xold; xold = x; gamma = xnew;
    % TEST CONVERGENCE
    if iter >= 100 | max(abs(gamma-xold)) < 0.01
        break
    end
    % UPDATE DESIGN VARIABLE
    u0 = fem.sol.u; u0(i4) = gamma;
    fem.sol = femsol(u0);
    % DISPLAY RESULTS FOR EACH ITERATION STEP
    disp(sprintf('Iter.:%3d Obj.: %8.4f Vol.: %6.3f Change: %6.3f', ...
        iter,f,xold'*Vgamma,max(abs(xnew-xold))))
    postplot(fem,'arrowdata',{ 'u' 'v' }, 'tridata','gamma','trimap','gray')
    axis equal; shg; pause(0.1)
end

```

#### ACKNOWLEDGEMENTS

We are grateful to Ole Sigmund and Allan Gersborg-Hansen for illuminating discussions on the topology optimization method, and to Krister Svanberg for providing us with the MATLAB code for the MMA algorithm. This work is partly supported by The Danish Technical Research Council, Grant No. 26-03-0037.

#### REFERENCES

1. Bendsøe MP, Kikuchi N. Generating optimal topologies in structural design using a homogenization method. *Computer Methods in Applied Mechanics and Engineering* 1988; **71**(2):197–224.
2. Bendsøe MP, Sigmund O. *Topology Optimization-Theory, Methods and Applications*. Springer: Berlin, 2003.
3. Eschenauer HA, Olhoff N. Topology optimization of continuum structures: a review. *Applied Mechanics Reviews* 2001; **54**(4):331–389.
4. Jensen JS. Phononic band gaps and vibrations in one- and two-dimensional mass-spring structures. *Journal of Sound and Vibration* 2003; **266**(5):1053–1078.
5. Jensen JS, Sigmund O. Systematic design of photonic crystal structures using topology optimization: low-loss waveguide bends. *Applied Physics Letters* 2004; **84**(12):2022–2024.
6. Borrvall T, Petersson J. Topology optimization of fluids in Stokes flow. *International Journal for Numerical Methods in Fluids* 2003; **41**:77–107.
7. Sigmund O, Gersborg-Hansen A, Haber RB. Topology optimization for multiphysics problems: a future FEMLAB application? In *Proceedings for the Nordic Matlab Conference 2003*, Gregersen L (ed.). Comsol A/S: Søborg, Denmark, 2003; 237–242.
8. Gersborg-Hansen A. Topology optimization of incompressible Newtonian flows at moderate Reynolds numbers. *M.Sc. Thesis*, Technical University of Denmark, Department of Mechanical Engineering, Lyngby, 2003.
9. Gersborg-Hansen A, Sigmund O, Haber RB. Topology optimization of channel flow problems. *Structural and Multidisciplinary Optimization* 2005. (Published online: DOI 10.1007/s00158-004-0508-7.)

10. Okkels F, Olesen LH, Bruus H. Applications of topology optimization in the design of micro- and nanofluidic systems. In *Proceedings of Nanotech*, vol. 1. Anaheim: CA, U.S.A., 2005; 575–578.
11. Svanberg K. The method of moving asymptotes—a new method for structural optimization. *International Journal for Numerical Methods in Engineering* 1987; **24**:359–373.
12. Svanberg K. A class of globally convergent optimization methods based on conservative convex separable approximations. *SIAM Journal on Optimization* 2002; **12**(2):555–573.
13. A MATLAB implementation, `mmasub`, of the MMA optimization algorithm [11] can be obtained (free of charge for academic purposes) from Krister Svanberg, KTH, Sweden. E-mail: [krille@math.kth.se](mailto:krille@math.kth.se)
14. Geschke O, Klank H, Telleman P (eds). *Microsystem Engineering of Lab-on-a-chip Devices*. Wiley-VCH Verlag: Weinheim, 2004.
15. Landau LD, Lifshitz EM. *Course of Theoretical Physics: Fluid Mechanics*, vol. 6 (2nd edn). Butterworth and Heinemann: Oxford, 2000.
16. Michaleris P, Tortorelli DA, Vidal CA. Tangent operators and design sensitivity formulations for transient non-linear coupled problems with applications in elastoplasticity. *International Journal for Numerical Methods in Engineering* 1994; **37**(14):2471–2500.
17. FEMLAB Reference Manual. COMSOL AB: Stockholm, 2004.
18. A simple implementation of a cone filter for dealing with mesh dependence problems on an unstructured triangular mesh in two dimensions with linear Lagrange elements for the design variable can be downloaded from <http://www.mic.dtu.dk/research/MIFTS>